THE ASTROPHYSICAL JOURNAL, 493:460–473, 1998 January 20

A TIME-DEPENDENT THREE-DIMENSIONAL MAGNETOHYDRODYNAMIC MODEL OF THE CORONAL MASS EJECTION

S. E. GIBSON[1] AND B. C. LOW
High Altitude Observatory, National Center for Atmospheric Research,[2] Boulder, CO 80307-3000

Received 1997 March 24; accepted 1997 August 6

ABSTRACT

We present a theoretical magnetohydrodynamic (MHD) model describing the time-dependent expulsion of a three-dimensional coronal mass ejection (CME) out of the solar corona. The model relates the white-light appearance of the CME to its internal magnetic field, which takes the form of a closed bubble, filled with a partly anchored, twisted magnetic flux rope, and embedded in an otherwise open background field. The model is constructed by solving in closed form the time-dependent ideal MHD equations for a $\gamma = 4/3$ polytrope making use of a similarity assumption and the application of a mathematical stretching transformation in order to treat a complex field geometry with three-dimensional variations. The density distribution frozen into the expanding CME magnetic field is obtained. The scattered white light integrated along the line of sight shows the conspicuous three features often associated with CMEs as observed with white-light coronagraphs: a surrounding high-density region, an internal low-density cavity, and a high-density core. We also show how the orientation of this three-dimensional structure relative to the line of sight can give rise to a variety of different geometric appearances in white light. These images generated from a CME model in a realistic geometry offer an opportunity to directly compare theoretical predictions on CME shapes with observations of CMEs in white light. The mathematical methods used in the model construction have general application and are described in the Appendices.

Subject headings: MHD — Sun: corona — Sun: particle emission

1. INTRODUCTION

Coronal mass ejections (CMEs) are episodic expulsions of mass and magnetic field from the solar corona into the solar wind (Crooker, Jocelyn, & Feynman 1997; Fisher 1984; Hildner 1992; Howard et al. 1985; Hundhausen 1988, 1995, Kahler 1992; Low 1990, 1996; MacQueen 1980). Each event produces a large-scale reconfiguration of the coronal magnetic field, and its expelled mass of about 10^{15} g is a significant perturbation in the solar wind. CMEs are one example of the ubiquitous magnetohydromagnetic (MHD) expulsion of mass from central bodies in the astrophysical universe, and are unique in that the proximity of the Sun allows us to observe the CME directly as a spatially resolved event; from preeruption, through the fully developed dynamical state, to the aftermath. The wealth of direct observational data shows that, in general, CMEs have finite lateral spatial extent, requiring a fully three-dimensional model to properly describe the observed phenomena. By "fully" we mean that there is variation with all three spatial dimensions without special symmetry. The purpose of this paper is to present such a three-dimensional MHD model to address issues of CME structure.

Mathematical problems dealing with fully three-dimensional magnetic fields are generally formidable, even with the use of numerical methods. This paper takes a substantive step toward the treatment of such problems in time-dependent mass expulsion. We will use a method of analytical construction that can produce exact MHD solutions for our use without the assumption of special symmetry. This method is interesting in its own right and has potential for greater applicability than employed here. In order to render it available for future use and not allow its details to detract from our physical motivation relating to CMEs, we have put the mathematical construction in Appendices A and B at the end of this paper. In the main text of the paper, we shall simply describe how the method produces the solutions that we will use to model the CME.

In § 2, we review the part of CME phenomenology relevant to the issues of magnetic structures in CMEs, leading to a set of requirements for the CME model presented in § 3. Our conclusion is given in § 4.

2. THE CME AND ITS MAGNETIC FIELD

CMEs are usually observed with a coronagraph, an instrument designed to observe the faint solar corona, normally visible only during a solar eclipse, by artificially occulting the solar disk. The coronal image thus formed registers photospheric white light Thomson-scattered into the line of sight [see Fig. 1 (Pl. 12)]. Because the light scatters off free coronal electrons, the brightness of coronal structures is a measure of the coronal electron density integrated along the line of sight (Billings 1966; Hundhausen 1993).

CMEs are transient events, but are intrinsically linked to long-lived, preexisting coronal structures. Figure 1 displays a time sequence of images, taken from the archive of the coronagraph on board the NASA *Solar Maximum Mission* (*SMM*) satellite, showing a CME in progress (Illing & Hundhausen 1986). In this sequence, a preexisting coronal helmet streamer is seen to break apart into an expanding structure that travels out of the corona at a speed of the order of 500 km s^{-1}. The mass in the leading looplike structure of the CME has been estimated to be of the order of 10^{15} g. The CME has a three-part structure: a bright leading loop, a dark cavity surrounded by the loop, and a high-density structure in the cavity, often in the form of an erupted prominence. This three-part structure may be iden-

---

[1] Laboratory for Astronomy and Solar Physics, NASA Goddard Space Flight Center.

[2] NCAR is sponsored by the National Science Foundation.

tified with a similar structure in the preexisting coronal helmet streamer: the high-density dome, the prominence cavity at the base of the dome, and the quiescent prominence in the cavity (Engvold 1989). A great many CMEs originate from the breakup of a helmet streamer and display the same characteristic three-part structure (Crifo, Picat, & Cailloux 1983; Hundhausen 1988). In some cases, especially those CMEs expelled from an active region, the cavity may contain an amorphous high-density core instead of the filamentary structures characteristic of an erupted prominence (Burkepile & St. Cyr 1993). It is unclear whether such amorphous cores are prominence materials which have lost their original filamentary structures or are of some other origin. It will be our hypothesis in this paper that the characteristic three-part structure observed in many cases is due to a common basic topological form of the magnetic fields in the CMEs.

Little direct observational knowledge of the coronal magnetic field exists. The corona at 2×10^6 K is so highly ionized that it is difficult to determine or detect the coronal magnetic field by spectroscopic means, as is done routinely for the photospheric field. Much of what is known about the coronal magnetic field is based on inference. Since the corona at its high temperature is practically a perfect electrical conductor, the plasma is constrained to move along the embedded magnetic lines of force, except in highly dissipative situations as during a flare (Parker 1979; Priest 1982). Therefore, the striations in solar plasma structures and the apparent channeling of moving plasmas are reasonably interpreted to be delineating bundles of magnetic line of force. Furthermore, the corona is generally thought to be dichotomized into regions where the field is closed or is open to interplanetary space (Hundhausen 1977). The former are the helmet streamers, and the latter are the regions between the helmet streamers, most notable of which are the coronal holes over the poles of the Sun during solar minimum. This physical picture is supported by the observed correlation between solar wind magnetic structures and the coronal holes interpreted to be their magnetic origin (Wang & Sheeley 1990; Zirker 1977).

In this manner, observations of coronal structures in white light or emission lines have historically been used to gain insight into the nature of the large-scale magnetic field in the corona (e.g., Altschuler & Newkirk 1969; Bagenal & Gibson 1991; Gibson & Bagenal 1995; Gibson, Bagenal, & Low 1996; Levine et al. 1977; Newkirk & Altschuler 1970; Schatten et al. 1969). For our CME model, we consider the white-light observations of CME eruptions and the preeruption corona in order to design an appropriate corresponding magnetic field structure.

2.1. *CME Precursors*

As mentioned above, a common CME precursor is the presence of a dark cavity located at the base of the helmet streamer, just above the polarity inversion line. In such a cavity, a prominence is often found (seen as an embedded sheet of plasma). In scattered white light, darkness implies absence of material, and we interpret the cavity as a region of locally enhanced magnetic fields whose magnetic pressure makes up for the deficit in gas pressure and thus keeps the cavity from inward collapse (Low 1980). Observation and modeling of the prominence and its cavity have led to the hypothesis that the cavity magnetic field is a rope of twisted magnetic flux, such as is sketched in Figure 2 (Low 1994; Low & Hundhausen 1995; Wu et al. 1995; Wu & Guo 1997). In the axisymmetric case sketched here, the magnetic flux rope is fully detached from the base of the corona and winds all the way around the Sun with a strong toroidal field component out of the meridional plane shown. It is surrounded by an arcade of bipolar field lines which have both ends anchored to the base, and this arcade is, in turn, surrounded by completely open, bipolar field lines. The flux rope is magnetically cut off from the photosphere, which is the source of mechanical power for heating and mass supply for the corona. This naturally explains why the thermodynamic state of the flux rope is dramatically different from the rest of the helmet. Shut off from the source of heating and mass, thermal condensation can take place readily in the flux rope, explaining the low density in the flux rope and the formation of the prominence within. (See Low & Hundhausen 1995 for further discussion.)

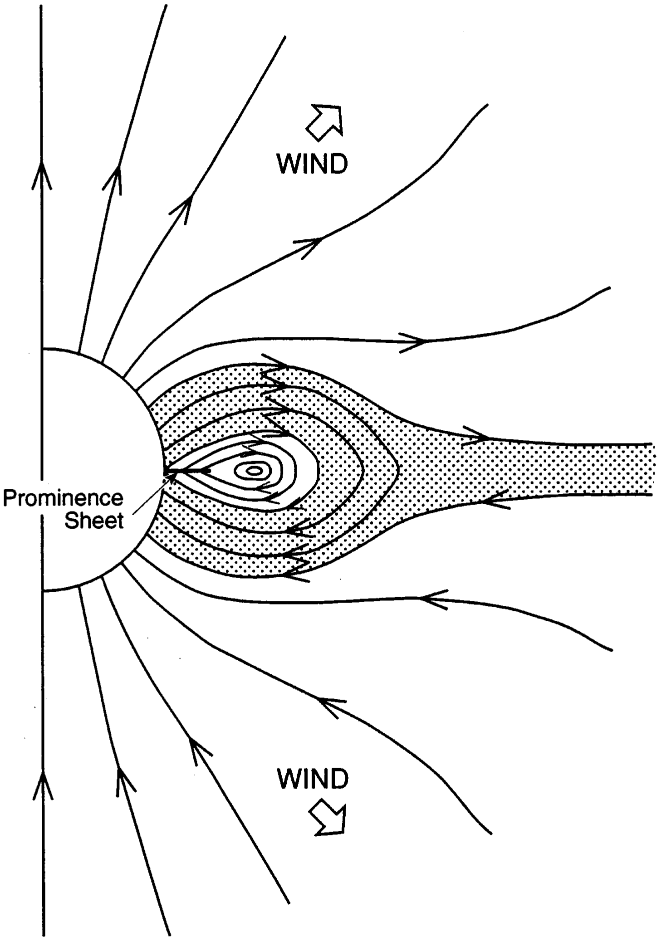

FIG. 2.—Sketch of the idealized solar corona taken to be symmetric about both the axis and the Equator of a large-scale dipolar magnetic field. As indicated by the arrowed lines of force, the corona is divided into an equatorial region of static closed fields sandwiched between the high-latitude open-field regions where the expanding solar wind flows. The closed region consists of a bipolar arcade of field lines, appearing in white light as a high-density dome blending into the streamer, and a cavity lying below this dome that is magnetically characterized here as a twisted magnetic flux rope entirely closed upon itself within the cavity and encircling the Sun above the magnetic Equator. The prominence is modeled as a sheet of material suspended inside the flux rope. The open magnetic field is poloidal, but an azimuthal field component is present in the magnetic fields which are either completely closed or anchored at the base, so that the arrowed lines for the latter are to be interpreted as lines of force projected onto the meridian plane (Low & Hundhausen 1995).

However, the axisymmetric case is a simplification. In the realistic three-dimensional situation, the fully detached flux rope in Figure 2 would be replaced by one whose two finite ends fold down to blend into some complex magnetic fields, connecting it to the photosphere. The field lines themselves, making up the flux rope, would be bipolar and anchored to the photosphere, differing from the overlying arcade of field lines by winding a few times about the flux rope axis between the two footpoints rather than making a more direct route from one footpoint to the other. The twisted rope is still thermodynamically isolated from the rest of the helmet streamer, because the longer thermal path length of the lines of force winding several times in the corona may promote condensation instabilities to form the prominence and the evacuated cavity (e.g., Smith & Priest 1977). Figure 2, with a strong enough azimuthal field component out of the meridian plane, may then be taken to depict the local field topology at a meridian plane through the midregion of the three-dimensional flux rope with finite ends anchored at the photosphere. A first approach to quantitative modeling, without relinquishing the essential three-dimensional topology of the magnetic field, is to treat the global dynamics of the CME in terms of integrated or net forces (e.g., Chen 1996). In this paper, we shall construct an exact solution to the complete set of time-dependent ideal MHD equations for the CME involving a three-dimensional flux rope, embedded in an external, open, bipolar magnetic field.

2.2. *CME Eruptions*

The structure of the CME itself is directly related to the structure of its helmet streamer precursor described above. In the 1990s, simultaneous observations of CMEs in white light and soft X-rays were conducted. White-light observations were conducted with the High Altitude Observatory (HAO) coronameter from the ground at Mauna Loa, and X-ray observations were provided by the instrument on the *Yohkoh* satellite. The latter was designed for studying the hot plasmas of flares at the high temperatures 2–3 million degrees (Ogawara et al. 1992). These simultaneous observations show few signatures in soft X-rays during the expulsion phase of a CME observed in full spectacular form in white light. Not until the CME has exited from the low corona does the X-ray instrument register the intense heating of the flare which often accompanies the CME as an aftereffect (Hiei, Hundhausen, & Sime 1994, 1997). This sequence of events has the simple theoretical interpretation that the CME is an ideal MHD expulsion process (Low 1994). When the CME has left the corona and the anchored part of the coronal magnetic field has been stretched out into a fully open state, resistive heating sets in as the result of magnetic reconnection to close the opened, bipolar magnetic field. This resistive heating as the origin of the so-called two-ribbon flare was suggested even before CMEs became well known (Hirayama 1974; Kopp & Pneuman 1976). Now, in the context of the CME, it can be considered to be the second step of a two-step process, the first being the opening of coronal magnetic fields by the CME (Hundhausen 1988; Low 1990). An important implication of this interpretation is that the basic magnetic field topology of the helmet is preserved in its ideal MHD breakup into a CME. Therefore, we expect the CME to have a stretched out but topologically the same magnetic field as inferred for the helmet, namely, one embedding a bipolar magnetic flux rope partially anchored to the coronal base. Outside the CME, the magnetic field is open and is pushed aside by the CME traveling out of the corona at typical speeds of about 500 km s^{-1}.

Although the CME is often expelled out of a long helmet-streamer belt overlying a polarity inversion line on the surface of the Sun, its own spatial extension is relatively limited. The distribution of latitudinal angular sizes of CMEs shows a range from 40° to 120° with a median of about 50°, based on the *SMM* coronagraph data set (Hundhausen 1993). Therefore, the model for a realistic CME must be a three-dimensional closed magnetic flux rope structure with a finite lateral spatial extension and initially embedded in an otherwise open, bipolar field. The time-dependent MHD motion of this embedded magnetic flux rope through the corona is the CME event. In the following section, we present such a CME model constructed with the analytical techniques developed in Appendices A and B.

3. THE THREE-DIMENSIONAL CME MODEL

The CME as an MHD phenomenon may be described by the following equations:

$$\rho\left[\frac{\partial \boldsymbol{v}}{\partial t} + (\boldsymbol{v}\cdot\nabla)\boldsymbol{v}\right] = \frac{1}{4\pi}(\nabla\times\boldsymbol{B})\times\boldsymbol{B} - \nabla p - \rho\,\frac{GM}{r^2}\,\hat{\boldsymbol{r}}\,, \quad (1)$$

$$\frac{\partial \rho}{\partial t} + \nabla\cdot(\rho\boldsymbol{v}) = 0\,, \quad (2)$$

$$\frac{\partial \boldsymbol{B}}{\partial t} = \nabla\times(\boldsymbol{v}\times\boldsymbol{B})\,, \quad (3)$$

$$\frac{\partial}{\partial t}(p\rho^{-\gamma}) + (\boldsymbol{v}\cdot\nabla)(p\rho^{-\gamma}) = 0\,, \quad (4)$$

for a polytropic plasma of index γ flowing with velocity $\boldsymbol{v}$ in a spherically symmetric gravitational field of a star and in the presence of a magnetic field $\boldsymbol{B}$. The corona is subject to heating and is an excellent thermal conductor. To retain a qualitative aspect of this heating while keeping the physics simple, we have assumed a polytropic gas to simulate a heated hydrogen gas by taking the polytropic index γ to have a value less than 5/3 for expansive motions.

Equations (1)–(4), suitably posed as an initial-boundary value problem, would describe the CME from its initiation in the preeruption corona to its passage out through the corona. This is a formidable problem treated in several recent numerical simulations under the assumption of axisymmetry. Mikic & Linker (1994) and Steinolfson (1988) treated the model in which a helmet streamer without the cavity flux rope is caused to open, as the result of photospheric displacements of the feet of anchored bipolar magnetic fields. While such a process is physically interesting in its own right (Low 1986, 1990; Wolfson & Low 1992; Klimchuk & Sturrock 1989; Wolfson, Bhattacharjee, & Dlamini 1996), its application to the CME has certain limitations pointed out in Low & Smith (1993) and Low (1997). From both observation and theoretical considerations, the cavity flux rope is an essential participant in the CME phenomenon (Low 1996). Numerical simulation of the CME in axisymmetric geometry, to explore the role of the cavity flux rope, has begun recently with a successful reproduction of the three-part structure of the observed CMEs (Wu, Guo, & Wang 1995; Wu & Guo 1997). Extension of this numerical work to three-dimensional geometry is important for application to the realistic CMEs.

Although the MHD equations generally require a numerical treatment, opportunities occasionally present themselves for treatment by analytical methods. These opportunities are valuable in allowing us to study physical properties in terms of close-form solutions. Such an opportunity is presented in this paper.

We are interested in the magnetic structures of CMEs during their fully developed motion through the corona. Many CMEs are observed to maintain their large-scale features with coherence during their motions. Therefore, a self-similar dynamical evolution is a first approach to the description of the CME (Low & Hundhausen 1987). This is the approach we take, yielding, as we shall see, an exact solution to the time-dependent equations (1)–(4) that is capable of modeling the three-dimensional complex magnetic fields of CMEs we might expect from observational considerations.

3.1. *Self-similar Magnetohydrodynamics*

It is shown in Low (1984) that equations (1)–(4) admit time-dependent solutions with the radially directed flow

$$\boldsymbol{v} = r \frac{1}{\Phi_{\rm ss}} \frac{d\Phi_{\rm ss}}{dt} \hat{\boldsymbol{r}} , \tag{5}$$

where $\Phi_{\rm ss}$ is a function of time described by

$$\left(\frac{d\Phi_{\rm ss}}{dt}\right)^2 = \frac{\eta\Phi_{\rm ss} - 2\alpha}{\Phi_{\rm ss}} , \tag{6}$$

η and α being constants. In this flow, the physical quantities evolve in a self-similar manner according to

$$\boldsymbol{B} = \frac{1}{\Phi_{\rm ss}^2} \boldsymbol{H}(\zeta, \theta, \phi) , \tag{7}$$

$$p = \frac{1}{\Phi_{\rm ss}^4} P(\zeta, \theta, \phi) , \tag{8}$$

$$\rho = \frac{1}{\Phi_{\rm ss}^3} D(\zeta, \theta, \phi) , \tag{9}$$

where the radial dependence is combined with time via the similarity variable

$$\zeta = \frac{r}{\Phi_{\rm ss}} . \tag{10}$$

The quantities given by equations (5) and (7)–(9) satisfy the transport equations (2)–(4) for arbitrary forms of $\boldsymbol{H}$, P, and D with the assumption of $\gamma = 4/3$. Equation (1) then reduces to the form

$$\frac{1}{4\pi} (\nabla_\zeta \times \boldsymbol{H}) \times \boldsymbol{H} - \nabla_\zeta P - D\left(\frac{GM}{\zeta^2} + \alpha\zeta\right)\hat{\boldsymbol{r}} = 0 , \tag{11}$$

describing a "magnetostatic" equilibrium state in the similarity space obtained by replacing r with ζ. One may interpret the transformation from real spacetime to the three-dimensional similarity space (ζ, θ, ϕ) as a noninertial transformation to a frame of reference in which the magnetized plasma appears to be static. The noninertial nature of the transformation manifests itself as a radially directed body force, characterized by constant amplitude α, in the "stationary" frame, acting in addition to the gravitational force, as shown in equation (11). Of course, this equation needs to be supplemented with the solenoidal condition

$$\nabla_\zeta \cdot \boldsymbol{H} = 0 . \tag{12}$$

In the above equations, we have introduced the gradient operator in the similarity space by denoting it with a subscript as shown. A solution to the time-dependent problem is generated by a solution to equations (11)–(12), for $\boldsymbol{H}$, P, and D. In terms of these quantities and the temporal function $\Phi_{\rm ss}$ defined by equation (6) with prescribed constants η and α, the physical solution is given by equations (5) and (7)–(9). Depending on the values of η and α, the outward expansion exhibits a variety of behaviors: accelerated expansion ($\alpha > 0$), decelerated expansion ($\alpha < 0$), and inertial expansion ($\alpha = 0$) (see discussion in Low 1982). An intuitive way of interpreting equation (11) is to take note from Low (1982) that in the self-similar flow, each fluid particle moves, in such a way that ζ is a constant on the particle. The coordinates θ and ϕ are also fixed on the particle because its motion is radial. The net force acting on the particle is represented by the term with amplitude α in equation (11) for a fixed set of values of ζ, θ, ϕ. This net force is radial and is outward, inward, or zero, respectively, for $\alpha > 0$, $\alpha < 0$, or $\alpha = 0$.

At the time the self-similar MHD theory discussed here was first developed (Low 1984), there were no obvious ways to solve the magnetostatic equations (11) and (12) in fully three-dimensional space. The combination of the special transformations derived in Appendices A and B provides a first opportunity to study fully three-dimensional, time-dependent magnetohydrodynamics by explicit solutions.

3.2. *A Method of Constructing Three-dimensional MHD Solutions*

For completeness of discussion within this section, we outline the principal steps of solution construction described in detail in Appendices A and B. The central idea of the construction is the following mathematical transformation. Take the magnetostatic equations describing magnetic field $\boldsymbol{b}$ and pressure Π in spherical coordinates r, θ, ϕ:

$$\frac{1}{4\pi} (\nabla \times \boldsymbol{b}) \times \boldsymbol{b} - \nabla\Pi = 0 , \tag{13}$$

$$\nabla \cdot \boldsymbol{b} = 0 , \tag{14}$$

and subject the solution to these equations to a geometric radial stretching described in Appendix A: $r \rightarrow r - a$, a being a constant. This is a strictly mathematical procedure which yields a solution ($\boldsymbol{B}$, p) satisfying the magnetostatic equations

$$\frac{1}{4\pi} (\nabla \times \boldsymbol{B}) \times \boldsymbol{B} - \nabla p - \rho F(r)\hat{\boldsymbol{r}} = 0 , \tag{15}$$

$$\nabla \cdot \boldsymbol{B} = 0 . \tag{16}$$

Equation (13) differs from equation (15), the latter having a centrally directed body force with a spherically symmetric density $F(r)$ in spherical coordinates. In the case of a static stellar atmosphere, for example, we may set

$$F = \frac{GM}{r^2} , \tag{17}$$

to describe the stellar gravitational field, G and M being Newton's constant and the stellar mass, respectively. Formulae relating ($\boldsymbol{b}$, Π) to ($\boldsymbol{B}$, p) are given in Appendix A.

To the extent that we are able to solve equation (13) in complex geometry, the transformation yields a solution to equation (15). From this point of view, this theory does not appear to be of great value because equation (13) is as formidable to solve as equation (15), except when a special symmetry exists. What makes this transformation useful is that it allows us to generate geometrically complex solutions of equation (15) from the much simpler, symmetric solutions to equation (13).

This advantage is exploited in Appendix B where a solution to equation (13) is derived for a global magnetic field composed of an open magnetic field $\boldsymbol{b}_{\text{ext}}$ surrounding a spherical region σ of radius r_0, centered in the equatorial plane at a distance r_1 from the coordinate origin. Figure 3 is a sketch of the geometric configuration. Within σ resides a closed magnetic field $\boldsymbol{b}_{\text{int}}$. Both $\boldsymbol{b}_{\text{ext}}$ and $\boldsymbol{b}_{\text{int}}$ are solutions to equation (13), each solved with a different assumption of special symmetry.

The field $\boldsymbol{b}_{\text{ext}}$ is required to be a potential field open to infinity, of opposite polarities in the northern and southern hemispheres, reversing polarity abruptly across the solar Equator. Its magnetic lines of force need to be everywhere tangential to the boundary of σ. The pressure associated with this field is uniform, since the potential field exerts no Lorentz force (see eq. [13]). We construct this potential field so that it is axisymmetric about a line lying in the equatorial plane (or Z-axis in Fig. 3), and is due to a magnetic monopolar source located at the origin with suitable other magnetic sources inside σ so that the boundary of σ, denoted by $\partial\sigma$, is a magnetic flux surface. This is a standard application of the method of inverse transformation in potential theory. To obtain the bipolar nature of the $\boldsymbol{b}_{\text{ext}}$, we reverse the direction of the field about the solar Equator. The result is a bipolar field that is open and potential in the two hemispheres, with an equatorial current sheet.

The field $\boldsymbol{b}_{\text{int}}$ inside σ is a nonpotential magnetic field in the form of a spherical ball of twisted magnetic fields in equilibrium with a pressure distribution. Such a solution may be constructed if it is taken to be symmetric about some given axis, as given in Lites et al. (1995). This is the solution we adopt for $\boldsymbol{b}_{\text{int}}$ with the axis of symmetry taken to lie on the X' axis in Figure 3. (Note, however, that because $\partial\sigma$ is a spherical flux surface, we are at liberty to rotate the entire (X', Y', Z') coordinate system with respect to the (X, Y, Z) frame with no problem for the superposition of the fields.)

Taken as a global solution to equation (13), the total pressure $\Pi + b^2/8\pi$ is not continuous across the boundary $\partial\sigma$ since the solutions inside and outside σ are unrelated. This means that the boundary $\partial\sigma$ is not in static equilibrium. However, at this stage of the construction, no density structure is provided for, since, in the absence of the centrally directed external force F, the static equation (13) does not involve the density. The solution so far has been created purely by a mathematical procedure to capture a desired global field topology (see Fig. 4 [Pl. 13]). This topology will be combined with the mathematical stretching transformation of Appendix A in order to arrive ultimately at a truly physical solution that satisfies all requirements of force equilibrium, including the continuity of the total pressure across all interfaces.

Thus, we take the global solution $\boldsymbol{b}$ and subject it to the stretching transformation $r \rightarrow r - a$. Under this transformation, $\boldsymbol{b}$ transforms as a divergence-free vector into $\boldsymbol{B}$ given by equations (A2)–(A4) and (A17). In the case of a scalar function, say $f(r)$, its transformation under $r \rightarrow r - a$ is

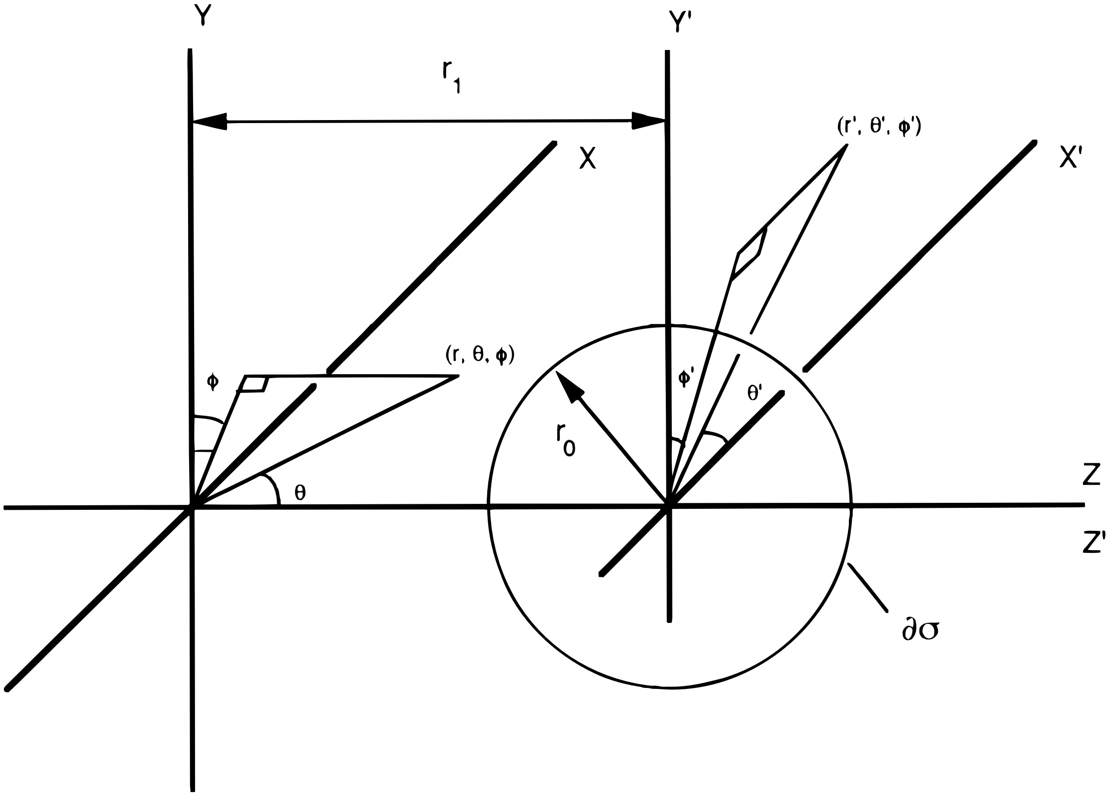

FIG. 3.—Cartesian systems (X, Y, Z) and (X', Y', Z'). The spherical coordinates (r, θ, ϕ) are defined with the Z-axis as the polar axis. The spherical coordinates (r', θ', ϕ') are defined with the X' axis as the polar axis. The surface σ is a sphere of radius r_0, centered on the (X', Y', Z') system.

simpler: if $g(r)$ is the transform of $f(r)$, then $g(r) = f(r + a)$. For $a > 0$, this transformation stretches space inward toward the origin. It effectively contracts the sphere of radius a, centered at the origin, to the point at the origin, and deforms the space outside this sphere symmetrically in all directions, with the contractive deformation diminishing at large r. As illustrated in Figure 5, this transformation takes the sphere σ to a tear-shaped region Σ. If the parameter a is chosen such that $a > r_1 - r_0$, a finite part of σ is contracted into the origin. If $a < r_1 - r_0$, Σ is a whole closed curve with no part of it contracted into the origin. The case shown in Figure 5 corresponds to the marginal case of $a = r_1 - r_0$ with the nearest point of the sphere σ pinched to locate right on the origin.

We denote the transform of $\boldsymbol{b}_{\text{ext}}$ and $\boldsymbol{b}_{\text{int}}$ by $\boldsymbol{B}_{\text{ext}}$ and $\boldsymbol{B}_{\text{int}}$, respectively. The stetching transformation does not preserve the detailed topology of the field acted upon by the transformation. Certain global topologies are preserved. It takes the original $\boldsymbol{b}_{\text{int}}$ confined in a spherically shaped region σ into another closed-field system $\boldsymbol{B}_{\text{int}}$ confined into the tear-shaped image volume Σ. The new flux surface $\partial\Sigma$ is still axisymmetric about Z, so we may rotate the coordinate system (X', Y', Z') about the Z-axis while Σ and $\partial\Sigma$ remain unchanged. Figure 6 (Plate 14) shows the transformed field corresponding to $a = r_1 - r_0$ projected into the Y-Z plane at two orientations of the inner solution (i.e., $X' \parallel X$ [Fig. 6*a*] and $X' \parallel Y$ [Fig. 6*b*]). From Figure 6 it is clear that the interior field $\boldsymbol{B}_{\text{int}}$ is no longer axisymmetric about the X' axis.

The transformed solution $\boldsymbol{B}_{\text{int}}$ satisfies equation (15), which introduces a density structure to be associated with the magnetic field. The exterior field $\boldsymbol{B}_{\text{ext}}$ also is now nonpotential with a density associated with it given by equation (15). The continuity of the total pressure across the surface $\partial\Sigma$ becomes crucial, since we now require this surface to be in force equilibrium. The magnetostatic equation (15) is linear in pressure and density. The combination of equations (4), (8), and (9) for $\gamma = 4/3$ imposes no relationship between P and D. This is a particular property of the self-similar flow given by equation (5) (Low 1984). Therefore, the pressure and density satisfying equation (15) may be adjusted by an arbitrary additive component, denoted by $p_0(r)$ and $\rho_0(r)$, respectively, such that

$$\frac{dp_0}{dr} + \rho_0 F(r) = 0 \; . \tag{21}$$

The free functions $p_0(r)$ and $\rho_0(r)$ may be chosen, as described below, to ensure that the total pressure is continuous across $\partial\Sigma$. The surface $\partial\Sigma$ is axisymmetric about the Z-axis of Figure 3, and the external field $\boldsymbol{B}_{\text{ext}}$ outside of it is also axisymmetric about the Z-axis. The internal $\boldsymbol{B}_{\text{int}}$ and its pressure have been constructed in such a way that they both vanish at the surface $\partial\Sigma$. Direct evaluation of the total pressure on the two sides of $\partial\Sigma$ then gives the jump of the total pressure on that surface. The axisymmetry of $\partial\Sigma$ about the Z-axis means that this total pressure jump is a function of the radial coordinate taken on $\partial\Sigma$. It then follows that if we introduce two suitable (different) profiles of p_0 and ρ_0 for the interior and exterior of Σ, the plasma pressure in the two regions may be adjusted in such a way that the total pressure is made continuous across $\partial\Sigma$. In this manner, the final solution obtained satisfies force equilibrium everywhere, inside and outside Σ and on the surface $\partial\Sigma$.

This is the global solution we shall take to be the solution to equation (11) in the similarity space (ζ, θ, ϕ), which upon transformation into physical spacetime gives a time-dependent self-similar solution to the MHD equations (1)–(4).

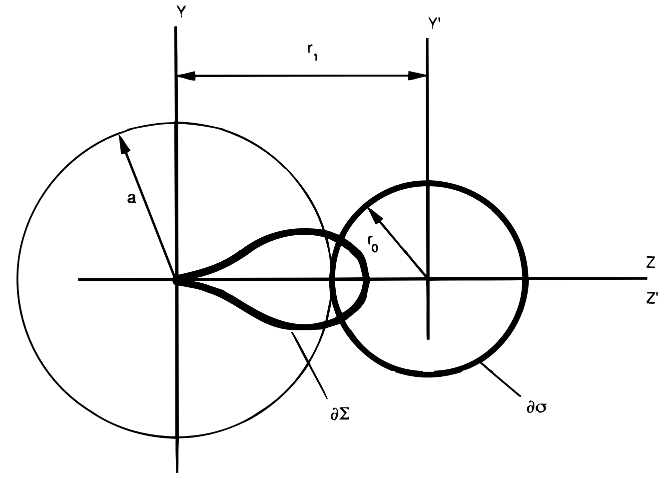

FIG. 5.—Limiting case $a = r_1 - r_0$, where the leftmost point of the circle is mapped exactly onto the origin. The mathematical stretching transformation takes a circle $\partial\sigma$ that is located in the Y-Z plane, of radius r_0, and displaced a distance r_1 from the origin, and maps it to the tear-shaped curve $\partial\Sigma$. This contraction "stretches" the space $r > a$ radially inward, under the transformation $r \rightarrow r - a$ (any points $r < a$ are collapsed onto the origin).

3.3. *The Global CME Model*

We are now ready to apply this model to the solar corona. The solution to equation (13) is obtained by combining the internal and external solutions ($\boldsymbol{b}_{\text{int}}$ and $\boldsymbol{b}_{\text{ext}}$) detailed in Appendix B. The solution to equation (15) is then obtained by using the stretching transformation $r \rightarrow r - a$ described in Appendix A with $a = r_1 - r_0/2$ (specifically, $a = 0.7$, $r_1 = 1.2$, $r_0 = 1.0$, and $a_1 = 0.23$). Finally this solution is applied to the similarity space via equation (11), and transformed to physical space through equations (6)–(10), to give a description of the time evolution of a model CME. We choose the case $\alpha = 0$ as the simplest example for the purpose of illustration. In this case the net force vanishes in the self-similar flow as can be seen by setting $\alpha = 0$ in equation (11) (α is defined in eq. [6]). Each particle of fluid moves at a constant Lagrangian speed. Different particles have different Lagrangian speeds, as described by the spatially varying Eulerian velocity. Thus $\Phi_{\text{ss}} = \eta^{1/2} t$, with $\eta = 1/3600^2$ chosen to normalize the timescales so that the speeds of the different parts of the model CME are of the order of a few hundred km s^{-1}, as observed of CMEs. For the parameters we have chosen, the constant Lagrangian velocity of the front of the CME is 580 km s^{-1}.

We take the polar axis for the Sun to be the Y-axis in the coordinate system of Figure 3. Thus, the global field is interpreted to be the heliospheric open bipolar field embedding a magnetic structure at the solar equator, which we take to be the closed field region of the CME. Figures 7 and 8 (Plates 15–18) show the evolving CME density and magnetic field structure seen projected in the plane of the sky and moving outward from the west (*right*) solar limb. Figure 7 shows the closed internal structure of the CME oriented so that $X' \parallel X$ in the coordinate system of Figure 3. The field structure contains a magnetic flux rope perpendicular to the plane of the sky, appearing here, centered at the solar equator, as a hole in the field lines (see particularly Fig. 7*d*). Figure 8 is oriented so that $X' \parallel Y$, so that the flux rope appears as a bundle of field lines twisted about an axis parallel to the solar limb (see particularly Fig. 8*d*).

We digress here to discuss an important point on the magnetic field topology displayed in Figures 7 and 8, in order to relate it to quiescent prominences. Returning to the simpler axisymmetric corona seen in Figure 2, note that in this model, the prominence is a long sheet of plasma embedded in a magnetic flux rope. This sheet is composed of cold plasma pieces residing at the gravitational bottoms of the concentric magnetic lines of force. This flux rope runs the length of the prominence. The magnetic structure in Figure 2 may be characterized to be one with two flux systems (Low & Hundhausen 1995). There is the flux system running along the prominence, oriented parallel to the photospheric polarity inversion line below. The second flux system corresponds to those magnetic fields anchored to the photosphere on the two sides of the polarity inversion line. In the axisymmetric geometry of Figure 2, the two fluxes are separate.

In the more realistic geometry of Figures 7 and 8, these two fluxes are linked into a stretched ball of magnetic fields, tethered to the origin, and described by the solution $\boldsymbol{B}_{\text{int}}$. In Figure 7, the twisted field winding around a local axis perpendicular to the plane of the sky gives a flux-rope structure aligned with this axis and appearing as a hole in the field lines. In Figure 8, the flux rope is located parallel to the solar limb. This flux rope can be identified with the part of the cavity which can embed a prominence (although we note that this model can only produce amorphous prominences rather than filamentary ones because of the simple form of the mathematical solution; see Lites & Low 1997). The flux rope is suspended in the atmosphere along the main part of its length, but at its ends, its field lines wind out of the rope and around to fill the rest of the volume and tether the bubble Σ to the photosphere. These less tightly wound field lines, which are identified with the second flux system, are anchored to the surface, and they lie on the torus-like surface seen most clearly in Figure 7.

A prominence-type enhancement does indeed appear embedded in the magnetic flux rope. The stretching transformation of the field has mathematically introduced magnetic tension forces requiring the introduction of corresponding gravitational and pressure forces to maintain static equilibrium in the (ζ, θ, ϕ) similarity space. Where magnetic valleys are stretched radially inward, added mass must be introduced whose weight can balance the tension force created by the stretching. The result is a local net density enhancement. Where convex field lines are stretched, out, a buoyant force is needed to balance the tension force created. The local result is a density-depleted cavity. A comparison of Figure 8*c* to Figure 8*d* shows that the field lines along the flux rope are primarily curved inward, cradling a density enhancement along the flux rope. The outer field lines are mainly pulled outward, requiring a buoyant cavity above the density enhancement. Figure 7*d* also shows the buoyant cavity, as well as a smaller end-on version of the density enhancement centered at the equator. The density enhancement around the bubble boundary between the internal and external solutions is created partly by the matching of the total pressure across the boundary $\partial\Sigma$. This three-part structure of a spheroidal front surrounding a cavity and a following dense core (which we can identify with a prominence) is, as discussed above, characteristic of many CMEs.

The density contours of Figures 7 and 8 are negative where there is a local depletion, and positive where there is a local enhancement, both measured relative to an unspecified background hydrostatic atmosphere. As we have stated, the linearity in p and ρ in the equilibrium equation allows for an arbitrary superposition of the solution with a spherically symmetric hydrostatic atmosphere. This arbitrary background atmosphere needs to be prescribed in such a way that the pressure and density of the final solution constructed are positive everywhere in the domain.

In order to appreciate the observational implications of the three-dimensionality of the density, we turn to polarized brightness (PB). This quantity PB is the Thomson-scattered, polarized component of the coronal brightness seen in Figure 1, and is a particularly useful observable because it is directly proportional to the integral along the line of sight of the electron density. Given a density distribution predicted by the model, and assuming a scattering function that takes into account the extended source of light of the solar disk as well as limb darkening, we can compute a model PB (Billings 1966). In the gray-scale image plots of Figures 9 and 10, we plot the model PB that a coronagraph would observe for the two orientations of the CME seen in Figures 7 and 8, respectively. The dark regions occur where the integral along the line of sight of the density shows net depletion, and bright regions lie where the net density integral is enhanced.

Figure 9 is particularly impressive in its qualitative reproduction of the essential features of the CME seen in Figure 1. The emergence of the three-part structure matches the emergence of a CME in the observation. The mass ejection begins with a bright circular front enclosing a cavity (Fig. 9*a*). Next an amorphous core emerges behind the cavity (Fig. 9*b*). The entire structure expands outward; leaving behind a V-shaped density enhancement where the "legs" of the ejection remain, as well as the remains of the bright core (Fig. 9*c*).

Figure 10 shows how different the same CME could appear if its magnetic axis were rotated about the Z axis, defined in Figure 3 so that the CME has a different orientation at the solar limb. The visibility of the bright core has been greatly diminished, but, on the other hand, the V-like structure seen in Figure 10*c* is more pronounced. The fact that the white-light coronagraph registers the integral along the line of sight of the density, coupled with the fact that the CME density is fundamentally a three-dimensional distribution, mean that very different white-light structures can arise from the different orientations of the CME structure. A rich variety of CME shapes is indeed observed (Burkepile and St. Cyr 1993).

3.4. *Discussion*

The solution we have constructed describes a global radial outflow that takes the entire atmosphere with its magnetic structure out to infinity. The Eulerian velocity is linear in the radial coordinate and, therefore, is divergent at large distance. This is not a concern because this self-similar solution is to be suitably matched through a transition layer moving ahead into the undisturbed corona (e.g., Low 1984). In the long-time limit, the self-similar velocity decays locally, and a static atmosphere is left behind. In this process, all magnetic structures not connected to the origin

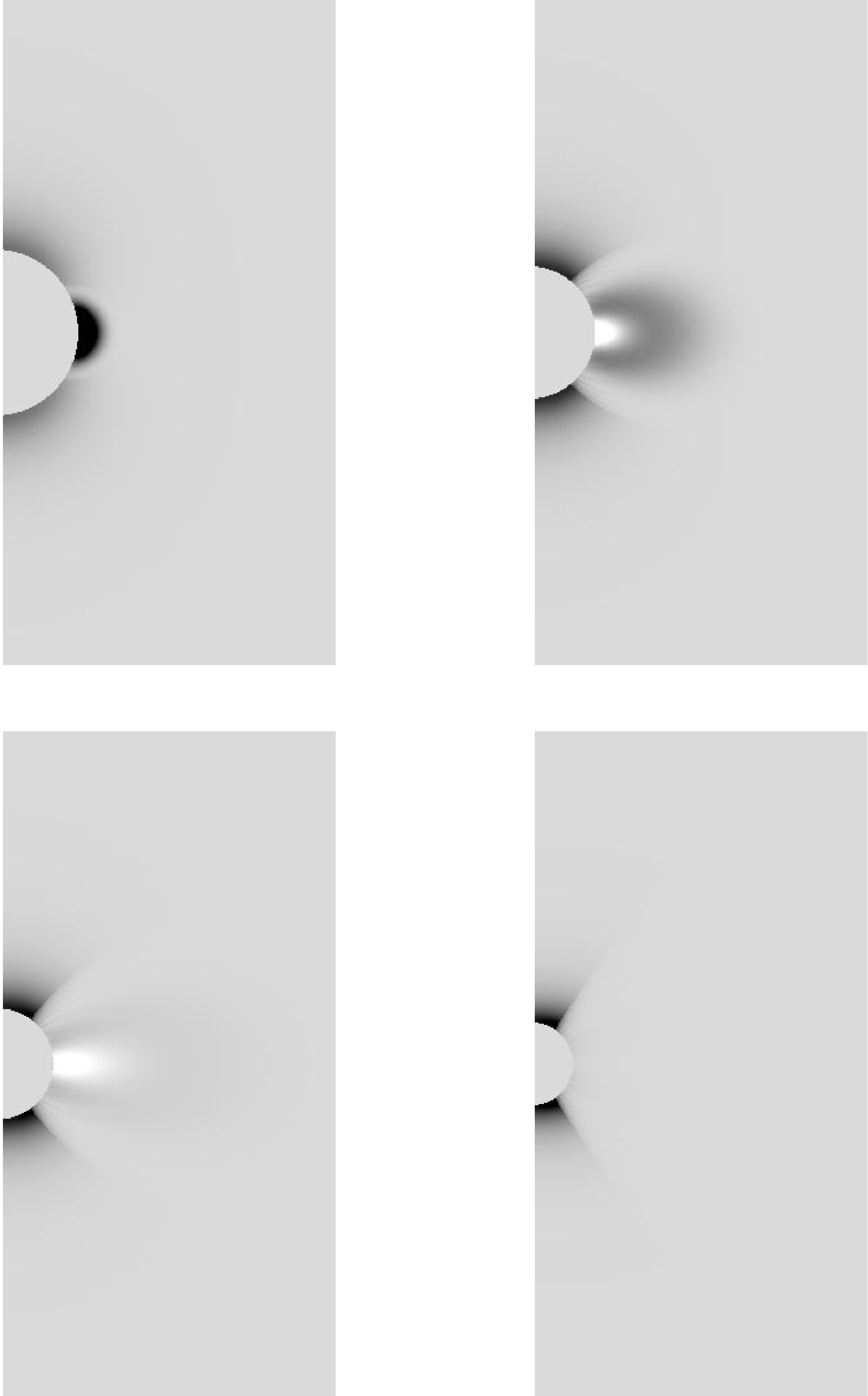

FIG. 9.—Self-similar evolution of CME solution for polarized brightness (PB), seen projected into the Y-Z plane. The bubble axis is seen oriented with $X' \parallel X$. Times correspond to the four time steps of Fig. 7.

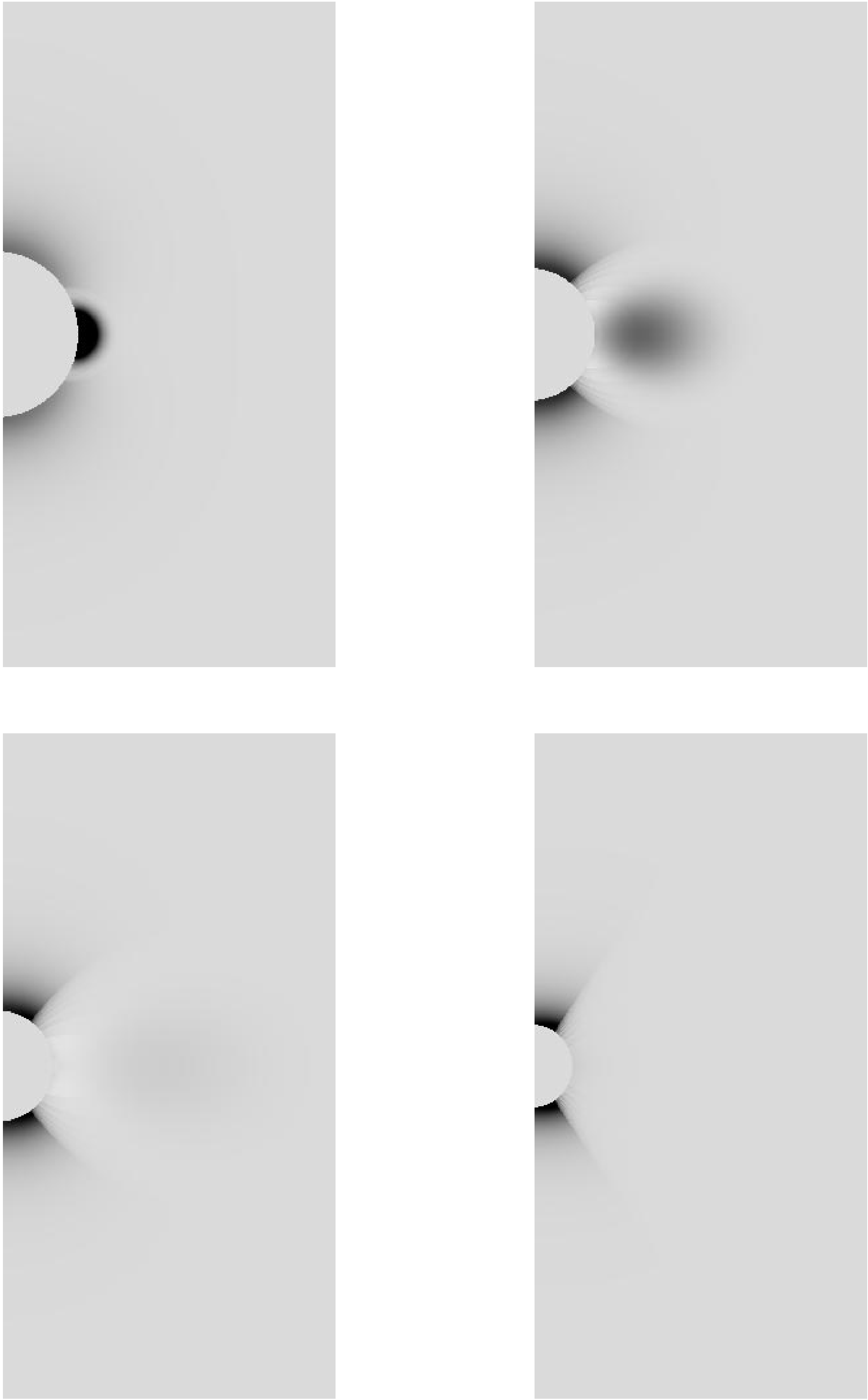

FIG. 10.—Self-similar evolution of CME solution for polarized brightness (PB), seen projected into the Y-Z plane. The bubble axis is seen oriented with $X' \parallel Y$. Times correspond to the four time steps of Fig. 8.

are taken out to infinity. Those magnetic structures which are connected to the origin remain connected in such a way that the magnetic field left behind is purely radial with a static polytropic atmosphere of index 4/3 in static equilibrium with it (Low 1984).

These properties of the solution need to be placed in the physical context of the initial-boundary value problem describing the whole process, from the CME initiation in a preexisting helmet-streamer structure to the post-CME flare involving resistive dissipation. Clearly the self-similar solution we have cannot be the proper solution to this complete initial-boundary value problem. Our solution can only be taken to describe a phase of evolution corresponding to the fully developed CME during its motion out of the corona. Moreover, our solution has to be taken to describe only the dynamics in a spatially limited domain, namely, from the atmospheric base out to the transition layer, possibly involving an MHD shock, propagating into the undisturbed far region (Low 1984). As the event proceeds, the appropriate boundary conditions at the base of the corona may not be compatible with what is required to maintain the self-similar motion, even if the motion has been set up initially to be self-similar. Thus, we expect the self-similar solution to evolve in time into a non–self-similar phase in response to the changing boundary conditions at the coronal base. One physical reason for this change would be the eventual depletion of coronal materials by the outflow from the base.

It is during the non–self-similar evolution after the CME has long left the coronal base when the magnetic field reversal layer of the opened bipolar field low in the corona would collapse as magnetic reconnection sets in to initiate the post-CME flare. Reconnection initiates low in the coronal base and proceeds to connect the opened lines of force until such a height where the solar wind flow is strong enough to keep the field open. This entire MHD process, within which the self-similar evolution is only a part, needs to be kept in mind. The self-similar model described in this paper makes assumptions neither regarding the initial triggering of the CME nor about eventual reconnection of the field lines. It is conceivable that a variety of CME initiation mechanisms may result in the self-similar evolution of a magnetic field/density structure such as the one we have constructed.

4. CONCLUSIONS AND FUTURE WORK

By direct construction, we have captured the essence of the CME as a closed magnetic field structure expanding and pushing its way through surrounding open magnetic fields anchored to the Sun. Observations of CMEs show a common occurrence of an ordered expansion during which the CME maintains an impressive coherent form, and we model this stage of their evolution under the assumption of self-similarity in time. By concentrating on the self-similar development, we are able to relate theoretically the density structure of the CME to its magnetic field in a self-consistent, fully three-dimensional MHD model.

In contrast to traditional models of CME magnetic fields, we model the closed magnetic field as a twisted magnetic flux rope and not a field consisting of simple bipolar fields (Low & Smith 1993; Wolfson et al. 1996; Wu et al. 1995). Such a twisted flux rope configuration has been shown to be compatible with observed bipolar distributions of normal magnetic flux on the solar surface $r = R_\odot$ (Lites et al. 1995). The evolution of the density structure corresponding to this magnetic structure captures many of the morphological and kinematic properties observed in CMEs. The often observed features of an enhancement around the CME, a cavity inside, and an enhanced core match observations, at least qualitatively. This result encourages us to believe that the basic magnetic structure of our model is an appropriate one to use in further study of CMEs. The core enhancement of this model is necessarily amorphous, rather than filamentary, because of the relative mathematical simplicity of the particular model we use. Nevertheless, the premise of magnetic valleys holding dense material is a general one. A more sophisticted model may be able to use field lines similar to those described by this model as a structure upon which to condense material of scale lengths more appropriate to observed prominence material, and so reproduce a more filamentary structure than those produced in our model (see Lites & Low 1997).

We plan in a future paper to demonstrate how the parameters of the model can be constrained by matching quantitative measurements of PB in CME observations. We can easily add a hydrostatic atmosphere in order to get the background corona if we wish, and can vary the parameters representing the size and location of the bubble (r_0, r_1), as well as those determining the relative importance of gas pressure and magnetic forces (a_1, a). We also plan to study how the CME would appear projected on the solar disk if we were to change our line of sight to one through the Sun center rather than tangent to the limb. The densities determined in this way might be used to predict coronal emission-line signatures of CMEs.

The duration of the CME event modeled here and the magnitude of its constant Lagrangian velocity of 580 km s^{-1} agree with observations reasonably well. This is not too surprising, as we were free to choose an appropriate timescale via the parameter η. We plan in our future analysis to vary the parameter α of the self-similar analysis (eq. [6]) which will allow acceleration (or deceleration) of the CME (see Low 1982 for a detailed discussion). Since CMEs appear to undergo some acceleration, particularly at the beginning of their emergence, this will be another parameter that can be fitted to observations.

The appearance of the CME varied significantly, depending upon the orientation of its magnetic flux rope axis. Observations of CMEs, even when limited to the large set of those with a three-part structure, show a rich variety of forms in white light. Therefore, two more parameters can be exploited to match observations, namely, the rotation of the entire CME structure away from the solar limb onto the solar disk, and the rotation of the CME around its own magnetic axis.

We have presented a first three-dimensional, time-dependent MHD model of CMEs that qualitatively matches observations and can in the future be constrained quantitatively by data. In doing so, we have come a step closer to understanding the magnetic nature of CMEs.

We would like to thank Andy Skumanich and Oscar Steiner for their helpful comments on this paper. This work was carried out during the terms of S. G. as Visiting Scientist at the HAO and as NASA-NRC Research Associate at Goddard Space Flight Center.

APPENDIX A

GENERAL METHOD FOR CONSTRUCTING MHD SOLUTIONS

To obtain the transformation taking a solution of equations (13) and (14) to a solution of equations (15) and (16), begin with the solenoidal condition (14) on $\boldsymbol{b}(r, \theta, \phi)$ in standard spherical coordinates:

$$\frac{1}{r^2}\frac{\partial}{\partial r}(r^2 b_r)+\frac{1}{r\sin\theta}\left[\frac{\partial}{\partial\theta}(\sin\theta\, b_\theta)+\frac{\partial b_\phi}{\partial\phi}\right]=0\,. \tag{A1}$$

Replace the independent argument r of $\boldsymbol{b}$ with a new variable $\Lambda(r)$, to be determined later, but leave the coordinates θ and ϕ unchanged. Henceforth, take $\boldsymbol{b}$ to be a function of Λ, θ, and ϕ, unless specified otherwise. If we define a new transformed magnetic field $\boldsymbol{B}$ in terms of $\boldsymbol{b}$ as follows,

$$B_r(r, \theta, \phi)=\left(\frac{\Lambda}{r}\right)^2 b_r(\Lambda, \theta, \phi)\,, \tag{A2}$$

$$B_\theta(\mathrm{r}, \theta, \phi)=\frac{\Lambda}{r}\frac{d\Lambda}{dr}\, b_\theta(\Lambda, \theta, \phi)\,, \tag{A3}$$

$$B_\phi(\mathrm{r}, \theta, \phi)=\frac{\Lambda}{r}\frac{d\Lambda}{dr}\, b_\phi(\Lambda, \theta, \phi)\,, \tag{A4}$$

direct substitution shows that

$$\nabla\cdot\boldsymbol{B}(r, \theta, \phi)=\left(\frac{\Lambda}{r}\right)^2\frac{d\Lambda}{dr}\,\nabla_\Lambda\cdot\boldsymbol{b}(\Lambda, \theta, \phi)\,, \tag{A5}$$

where we have introduced the operator

$$\nabla_\Lambda=\left(\frac{\partial}{\partial\Lambda}, \frac{1}{\Lambda}\frac{\partial}{\partial\theta}, \frac{1}{\Lambda\sin\theta}\frac{\partial}{\partial\phi}\right). \tag{A6}$$

It follows that if $\boldsymbol{b}(\Lambda, \theta, \phi)$ is solenoidal in the (Λ, θ, ϕ)-space, so is $\boldsymbol{B}(r, \theta, \phi)$ in the physical (r, θ, ϕ)-space as given by equations (A2)–(A4), for any transformation Λ.

Now suppose $\boldsymbol{b}$ satisfies equation (13) for some suitable pressure distribution Π in the (Λ, θ, ϕ) space. Writing this equation explicitly in the (Λ, θ, ϕ)-space, we have

$$\frac{1}{4\pi}\,\boldsymbol{b}\cdot\nabla_\Lambda b_r-\frac{1}{4\pi\Lambda}(b_\theta^2+b_\phi^2)-\frac{\partial}{\partial\Lambda}\left(\Pi+\frac{b^2}{8\pi}\right)=0\,, \tag{A7}$$

$$\frac{1}{4\pi}\,\boldsymbol{b}\cdot\nabla_\Lambda b_\theta+\frac{1}{4\pi\Lambda\sin\theta}(b_\theta b_r\sin\theta-b_\phi^2\cos\theta)-\frac{1}{\Lambda}\frac{\partial}{\partial\theta}\left(\Pi+\frac{b^2}{8\pi}\right)=0\,, \tag{A8}$$

$$\frac{1}{4\pi}\,\boldsymbol{b}\cdot\nabla_\Lambda b_\phi+\frac{1}{4\pi\Lambda\sin\theta}\,b_\phi(b_r\sin\theta+b_\theta\cos\theta)-\frac{1}{\Lambda\sin\theta}\frac{\partial}{\partial\phi}\left(\Pi+\frac{b^2}{8\pi}\right)=0\,. \tag{A9}$$

where we take Π to be a function of Λ, θ, and ϕ. It is straightforward to derive from equations (A2)–(A4) that

$$\boldsymbol{B}\cdot\nabla B_r=\left(\frac{\Lambda}{r}\right)^4\frac{d\Lambda}{dr}(\boldsymbol{b}\cdot\nabla_\Lambda b_r)+\frac{\Lambda^2}{r^2}\frac{d}{dr}\left(\frac{\Lambda^2}{r^2}\right)b_r^2\,, \tag{A10}$$

$$\boldsymbol{B}\cdot\nabla B_\theta=\left(\frac{\Lambda}{r}\right)^3\left(\frac{d\Lambda}{dr}\right)^2(\boldsymbol{b}\cdot\nabla_\Lambda b_\theta)+\left(\frac{\Lambda}{r}\right)^2\frac{d}{dr}\left(\frac{\Lambda}{r}\frac{d\Lambda}{dr}\right)b_r b_\theta\,, \tag{A11}$$

$$\boldsymbol{B}\cdot\nabla B_\phi=\left(\frac{\Lambda}{r}\right)^3\left(\frac{d\Lambda}{dr}\right)^2(\boldsymbol{b}\cdot\nabla_\Lambda b_\phi)+\left(\frac{\Lambda}{r}\right)^2\frac{d}{dr}\left(\frac{\Lambda}{r}\frac{d\Lambda}{dr}\right)b_r b_\phi\,. \tag{A12}$$

Using equations (A8) and (A9), it follows from equations (A11) and (A12) that

$$\frac{1}{4\pi}\,\boldsymbol{B}\cdot\nabla B_\theta+\frac{1}{4\pi r\sin\theta}(B_\theta B_r\sin\theta-B_\phi^2\cos\theta)-\frac{1}{r}\frac{\partial}{\partial\theta}\left[\left(\frac{\Lambda}{r}\frac{d\Lambda}{dr}\right)^2\left(\Pi+\frac{b^2}{8\pi}\right)\right]=\frac{b_\theta b_r}{4\pi}\left(\frac{\Lambda}{r}\right)^3\frac{d^2\Lambda}{dr^2}\,, \tag{A13}$$

$$\frac{1}{4\pi}\,\boldsymbol{B}\cdot\nabla B_\phi+\frac{1}{4\pi r\sin\theta}(B_\phi B_r\sin\theta+B_\theta B_\phi\cos\theta)-\frac{1}{r\sin\theta}\frac{\partial}{\partial\phi}\left[\left(\frac{\Lambda}{r}\frac{d\Lambda}{dr}\right)^2\left(\Pi+\frac{b^2}{8\pi}\right)\right]=\frac{b_\phi b_r}{4\pi}\left(\frac{\Lambda}{r}\right)^3\frac{d^2\Lambda}{dr^2}\,, \tag{A14}$$

For the magnetic field $\boldsymbol{B}$ to satisfy the magnetostatic equation (15), a comparison of the θ- and ϕ-components of equation (15) with equations (A13) and (A14), respectively, leads to the requirements

$$\left(\frac{\Lambda}{r}\frac{d\Lambda}{dr}\right)^2\left(\Pi+\frac{b^2}{8\pi}\right)=p+\frac{B^2}{8\pi}\,, \tag{A15}$$

$$\frac{d^2\Lambda}{dr^2} = 0 \; . \tag{A16}$$

Equation (A16) has the complete integral

$$\Lambda = kr + a \; , \tag{A17}$$

where k and a are arbitrary constants. Using the solution for Λ and equations (A2)–(A4), we rewrite equation (A15) to express the pressure p in terms of $\boldsymbol{b}$ and Π:

$$p = \frac{\Lambda^2}{r^2}\left(k^2 - \frac{\Lambda^2}{r^2}\right)\left(\frac{b_r^2}{8\pi}\right) + \frac{\Lambda^2}{r^2}\, k^2 \Pi \; . \tag{A18}$$

We can now use the r-component of equation (15) to obtain the expression for the equilibrium density:

$$\rho = \frac{1}{F(r)}\left[-\frac{\Lambda^2}{r^2}\, k\left(k^2 - \frac{\Lambda^2}{r^2}\right)\frac{d}{d\Lambda}\left(\Pi + \frac{b^2}{8\pi}\right) + 2\,\frac{\Lambda}{r}\,\frac{ak^2}{r^2}\,\Pi + \frac{1}{4\pi}\,\frac{\Lambda}{r}\,\frac{a}{r^2}\left(k^2 - 2\,\frac{\Lambda^2}{r^2}\right)b_r^2 + \frac{\Lambda^2}{r^2}\, k\left[\frac{a^2}{r^2} + \frac{2ka}{r}\right]\left[\frac{b_\theta^2 + b_\phi^2}{4\pi\Lambda}\right]\right] . \tag{A19}$$

The derivation is now complete. Given a solution $\boldsymbol{b}$ and Π of equations (13) and (14), we can construct a solution to equations (15) and (16) by first transforming coordinate systems by substituting Λ (as given by eq. [A17]) for the radial coordinate r, in the expressions for $\boldsymbol{b}$ and Π. The results are substituted into equations (A2)–(A4), (A18), and (A19), to determine $\boldsymbol{B}$, p, and ρ, respectively. In the analysis of this paper, we have set $k = 1$, since varying k merely scales the entire system.

If the force density $F(r)$ is the gravitational field of a star, as given by equation (17), $\boldsymbol{B}$, p, and ρ describe a static atmosphere in which the Lorentz force balances the pressure gradient and gravitational forces. In principle, the pressure and density are related by an independent equation for steady energy balance: equation (15) and the solenoidal condition together pose four equations for five unknowns (namely, the three components of $\boldsymbol{B}$, along with p and ρ), and so require an additional equation to close the system. In the above construction, the solution to the well-posed problem of four equations (i.e., eqs. [13] and [14]) in four unknowns ($\boldsymbol{b}$, Π) is transformed to a solution of the underdeterminate system (i.e., eqs. [15] and [16]) in the five unknowns ($\boldsymbol{B}$, p, and ρ) by relating $\boldsymbol{B}$ to $\boldsymbol{b}$ through the coordinate Λ. The underdeterminate system is effectively closed by the prescription of the functional form of Λ (eq. [A17]). Given that the fully three-dimensional magnetostatic problem is very complex and poorly understood, it is reasonable to ignore the demand of energy balance and use the above transformation as a means of generating equilibrium states for studies that concentrate on exploring magnetic morphologies rather than the precise mechanism of energy balance in a given physical situation. This is the basic motivation of the approach taken here and elsewhere.

There is one circumstance under which the underdeterminacy of equations (15) and (16) is physically quite meaningful. This is the case of the self-similar time dependent expansion of the $\gamma = 4/3$ polytropic plasma (Low 1984), which conserves its entropy-like quantity

$$s = p\rho^{-4/3} \; , \tag{A20}$$

It is shown in Low (1982) that the velocity given by equation (5) describes Lagrangian motions of particles in the flow which keep the radial coordinate ζ, given by equation (10), constant on each particle. Hence, s cannot depend on time except through ζ. Once each particle is given a value of s in the flow, it remains unchanged, but that value can be arbitrarily prescribed. Hence, while equation (A20) serves to physically close equations (15) and (16), there is no mathematical closure because s is an arbitrarily prescribed function. By prescribing the form of Λ in equation (A17) we mathematically close the system, and when this solution is transformed to the self-similar system, the choice of Λ corresponds physically to a choice of self-consistent " entropy " distribution in the time-dependent magnetohydrodynamic flow.

APPENDIX B

GLOBAL SOLUTION TO EQUATION (13)

Our global solution consists of an open magnetic field surrounding a self-contained spherical region σ of closed magnetic field. The region σ has radius r_0, and is centered a distance r_1 from the origin of the open field. Figure 3 shows the coordinate systems we will use in our construction: (X, Y, Z) is the Cartesian system associated with the spherical coordinates (r, θ, ϕ), and (X', Y', Z') is the Cartesian system centered at the center of the sphere σ, associated with the spherical coordinates (r', θ', ϕ').

B1. MAGNETOSTATIC SOLUTION OUTSIDE σ: $\boldsymbol{b}_{\text{ext}}$

To construct the external potential field with lines of force anchored at one end at the origin and streaming out to infinity without penetrating the sphere σ, we look for a solution symmetric about the Z axis. The streaming magnetic flux can be accounted for by placing a monopolar magnetic source at the origin. However, since the surface of the sphere, $\partial\sigma$, needs to be a magnetic flux surface, it follows that the magnetic source at the origin must be superposed with other sources inside σ which are its inverse images. This works out mathematically as follows (Chou & Low 1994).

We write the magnetic field in terms of the stream function A:

$$\boldsymbol{b}_{\text{ext}} = \frac{1}{r \sin \theta}\left(\frac{1}{r}\frac{\partial A}{\partial \theta}\,\hat{\boldsymbol{r}} - \frac{\partial A}{\partial r}\,\hat{\boldsymbol{\theta}}\right) . \tag{B1}$$

The stream function for the potential field due to the monopolar source at the origin is

$$\Psi_0 = \cos \theta . \tag{B2}$$

The method of images gives the image Ψ_1 of Ψ_0 by inversion about the sphere $\partial\sigma$:

$$\Psi_1 = -\frac{1}{r_0}\,\frac{r_1(r^2 + r_1^2 - r_0^2) + r \cos \theta(r_0^2 - 2r_1^2)}{[(r_0^2 - r_1^2)^2 + r_1^2 r^2 + 2rr_1(r_0^2 - r_1^2) \cos \theta]^{1/2}} . \tag{B3}$$

The sum $\Psi_0 + \Psi_1 = 0$ on the surface $\partial\sigma$ so that this sphere is a flux surface of $\Psi_0 + \Psi_1$. The potential field generated by Ψ_1 is, however, singular along the axis of symmetry (the Z-axis in Fig. 3). These singularities correspond to a distribution of magnetic monopolar sources along the axis of symmetry. This peculiarity arises because the image within σ of a monopolar field cannot be a pure monopolar field. To remove these singularities outside σ, we introduce one other potential stream function Ψ_2 for superposition. Direct calculation gives

$$\Psi_2 = \frac{1}{r_0}\,(r^2 + r_1^2 - 2rr_1 \cos \theta)^{1/2} . \tag{B4}$$

This stream function is its own self-image, ensuring that the sphere of inversion σ remains a flux surface. This potential Ψ_2 is able to cancel out the singularities along the axis of symmetry introduced by Ψ_1, except for a small region along the axis of symmetry in the southern hemisphere within the bubble bounded by $\partial\sigma$. Because the singularity of the total solution

$$A = \Psi_0 + \Psi_1 + \Psi_2 \tag{B5}$$

is restricted to within σ, where we will be replacing the potential field by a different internal solution, it is enough that the potential field generated by A is everywhere regular outside σ. To convert the monopolar field outside σ to the global dipolar field, we may simply flip the sign of the field in either the northern or southern hemisphere of the Sun, defined so that the Y-axis in Figure 3 is taken to be the solar polar axis. Then the discontinuity of the field across the solar equator gives the equatorial current sheet operating the bipolar fields in the two hemispheres.

Since the outer magnetic field is potential, the gas pressure Π in equation (13) may be taken to be zero for this outer solution.

B2. MAGNETOSTATIC SOLUTION INSIDE σ: $\boldsymbol{b}_{\text{int}}$

We seek an inner solution satisfying equation (13) that describes a torus of magnetic flux wholly contained inside the sphere σ. To keep the mathematical problem tractable, we look for a solution which is axisymmetric about the X' axis at the center of the sphere σ in Figure 3. The desired solution is taken from the Appendix of Lites et al. (1995), first developed to simulate the emergence of a δ-sunspot into the photosphere. This solution describes a magnetic field

$$\boldsymbol{b}_{\text{int}} = \frac{1}{r' \sin \theta'}\left(\frac{1}{r'}\frac{\partial A}{\partial \theta'}\,\hat{\boldsymbol{r}}' - \frac{\partial A}{\partial r'}\,\hat{\boldsymbol{\theta}}' + \alpha_0 A\hat{\boldsymbol{\phi}}'\right) , \tag{B6}$$

$$A = \frac{4\pi a_1}{\alpha_0^2}\left[\frac{r_0^2}{g(\alpha_0 r_0)}\, g(\alpha_0 r') - r'^2\right] \sin^2 \theta' , \tag{B7}$$

where

$$g(\alpha_0 r') = \frac{\sin (\alpha_0 r')}{\alpha_0 r'} - \cos (\alpha_0 r') , \tag{B8}$$

with α_0 restricted, for a given r_0, by

$$J_{5/2}(\alpha_0 r_0) = 0 , \tag{B9}$$

involving the Bessel function in standard notation. The spherical coordinates (r', θ', ϕ') are associated with the Cartesian system (X', Y', Z') with the X' axis taken as the axis of symmetry. We will use the smallest eigenvalue of $\alpha_0 r_0 = 5.763854$.

The inner magnetic field can be calculated from its stream function using equation (B6) to calculate $\boldsymbol{b}_{r'}$, $\boldsymbol{b}_{\theta'}$, and $\boldsymbol{b}_{\phi'}$. The gas pressure is given by

$$\Pi = a_1 A . \tag{B10}$$

B3. GLOBAL SOLUTION: $\boldsymbol{b}$

We create the global solution for the magnetic field by linearly superposing the inner solution $\boldsymbol{b}_{\text{int}}$ inside σ and the outer solution $\boldsymbol{b}_{\text{ext}}$ outside σ, and rewriting the entire combined solution in terms of the coordinate system (r, θ, ϕ). Although each of the two solutions is axisymmetric in its own domain, the two axes of symmetry are perpendicular to each other (see Fig. 3). Hence, the composed global solution is not axisymmetric. Each solution satisfies equation (13), but because they are quite separate solutions, they do not have the same total pressure—magnetic plus plasma pressures—at the interface $\partial\sigma$. The internal solution has been constructed in such a way that the stream function A and its derivatives are zero on the bubble boundary (Lites et al. 1995). Since the inner-solution pressure Π is proportional to A, the total pressure of the internal solution vanishes on $\partial\sigma$. The outer solution has zero pressure but gives a nonvanishing magnetic pressure at $\partial\sigma$. There is then no way for the total pressure to be continuous across $\partial\sigma$. This implies that equilibrium is obtained everywhere except at the interface. However, this physical limitation is not crucial at this stage of the construction, as explained in the text.

Figure 4 shows the magnetic lines of force projected onto the Y-Z plane. Figure 4*a* shows the internal solution oriented as in Figure 3, with $X' \parallel X$, $Y' \parallel Y$, and $Z' \parallel Z$. Since $\partial\sigma$ is a spherical flux surface, we can rotate the entire internal (X', Y', Z') system with respect to the X, Y, Z) system without affecting the geometry of Σ and $\partial\Sigma$. Figure 4*b* shows the internal solution rotated about the Z-axis so that $X' \parallel Y$, $Y' \parallel X$, and $Z' \parallel Z$. The internal solution is now symmetric about $X' \parallel Y$. We perform this rotation to reveal the variation of the field of three dimensions in Figure 4. Note in particular the "flux rope" made by the helical field lines winding about the axis of symmetry: it appears as a hole in the field lines in Figure 4a, and as a twisted bundle of field lines in Figure 4*b*. The mathematical rotation of the internal solution relative to the fixed external field will also be used as a model parameter of the final, physical CME construction, to control how the orientation of the CME magnetic structure can affect its appearance as observed in white light.

REFERENCES

Altschuler, M. D., & Newkirk G. 1969, Sol. Phys., 9, 131

Bagenal, F., & Gibson S. E. 1991, J. Geophys. Res., 96, 17663

Billings, D. E. 1966, A Guide to the Solar Corona (San Diego: Academic)

Burkepile, J. T., & St. Cyr, O. C. 1993, NCAR Tech. Note TN-369+STR (Boulder: NCAR Publ.)

Chen, J. 1996, J. Geophys. Res., 101, 27499

Chou, Y. P., & Low, B. C. 1994, Sol. Phys., 153, 255

Crifo, F., Picat, J. P., & Cailloux, M. 1983, Sol. Phys., 83, 143

Crooker, N., Joselyn, J., & Feyman, J. (eds.) 1997, Coronal Mass Ejections (Washington DC: Amer. Geophys. Union)

Engvold, O. 1989, Dynamics and Structures of Quiescent Prominences, ed. E. R. Priest (Dordrecht: Kluwer), 47

Fisher, R. R. 1984, Adv. Space Res., 4, 163

Gibson, S. E., & Bagenal, F. 1995, J. Geophys. Res., 100, 19 865

Gibson, S. E., Bagenal, F., & Low, B. C. 1996, J. Geophys. Res., 101, 4813

Hiei, E., Hundhausen, A. J., & Sime, D. G. 1994, Geophys. Res. Lett., 20, 2785

———. 1997, in preparation

Howard, R. A., Sheeley, N. R., Jr., Koomen, M. J., & Michels, D. J. 1985, J. Geophys. Res., 90, 8173

Hildner, E. 1992, Eruptive Solar Flares, ed. A. Svestka, B. V. Jackson, & M. E. Machado (Berlin: Springer), 227

Hirayama, T. 1974, Sol. Phys., 34, 323

Hundhausen, A. J. 1977, Coronal Holes and High Speed Wind Streams, ed. J. B. Zirker (Boulder: Colorado Assoc. Univ. Press), 225

———. 1988, in Proc. Sixth International Solar Wind Conference, ed. V. Pizzo, D. G. Sime, & T. E. Holzer, NCAR TN-306; (Boulder: NCAR Publ.), 181

———. 1993, J. Geophys. Res., 98, 13177

———. 1995, The Many Faces of the Sun, ed. K. Strong, J. Saba, & B. Haisch, in press

Illing, R. M. E., & Hundhausen, A. J. 1986, J. Geophys. Res., 91, 10951

Kahler, S. 1992, ARA&A, 30, 113

Klimchuk, J., & Sturrock, P. A. 1989, ApJ, 345, 1034

Kopp, R., & Pneuman, G. W. 1976, Sol. Phys., 50, 85

Levine, R. H., Altschuler, M. D., Harvey, J. W., & Jackson, B. V. 1977, ApJ, 215, 635

Lites, B. W., et al. 1995, ApJ, 446, 877

Lites, B. W., & Low, B. C. 1997, Sol. Phys., 174, 91

Low, B. C. 1980, Sol. Phys., 65, 147

———. 1982, ApJ, 254, 796

———. 1984, ApJ, 281, 392

———. 1986, ApJ, 307, 205

———. 1990, ARA&A, 28, 491

———. 1994, Plasma Phys., 1, 1684

———. 1996, Sol. Phys., 167, 217

———. 1997, Coronal Mass Ejections, ed. N. Crooker, J. Joselyn, & J. Feynman (Washington DC: Amer. Geophys. Union), 39

Low B. C., & Hundhausen, A. J. 1987, J. Geophys., Res., 92, 2221

Low, B. C., & Hundhausen, J. R. 1995, ApJ, 443, 818

Low, B. C., & Smith, D. F. 1993, ApJ, 410, 412

MacQueen, R. M. 1980, Philos. Trans. R. Soc. London, A, 297, 605

Mikic, Z., & Linker, J. A. 1994, ApJ, 430, 898

Newkirk, G., & Altschuler, M. D. 1970, Sol. Phys., 9, 131

Ogawara, Y., et al. 1992, PASJ, 44, L41

Parker, E. N. 1979, Cosmical Magnetic Fields (Oxford: Oxford Univ. Press)

Priest, E. R. 1982, Solar Magnetohydrodynamics (Dordrecht: Reidel)

Schatten, K. H., Wilcox, J. M., & Ness, N. 1969, Sol. Phys., 6, 442

Smith, E. A., & Priest, E. R. 1977, Sol. Phys., 53, 25

Steinolfson, R. 1988, J. Geophys. Res., 93, 14261

———. 1991, ApJ, 382, 677

Wang, Y.-M., & Sheeley, N. R., Jr. 1990, ApJ, 355, 726

Wolfson, R., & Low, B. C. 1992, ApJ, 391, 353

Wolfson, R., Bhattacharjee, H., & Dlamini, B. 1996, ApJ, 463, 359

Wu, S. T., & Guo, W. P. 1997, ApJ, in press

Wu, S. T., Guo, W. P., & Wang, J. F. 1995, Sol. Phys., 157, 325

Zirker, J. B., ed. 1977, Coronal Holes and High Speed Wind Streams (Boulder: Colorado Assoc. Univ. Press)